Numerical Solution of Two-Dimensional Compressible Radiating Flowfields

Yih-Kanq Chen,* Philip L. Varghese,† and John R. Howell‡
The University of Texas at Austin, Austin, Texas 78712

A two-dimensional numerical model for flows with coupled radiation from an emitting, absorbing, and scattering fluid is developed. The continuity, momentum, and energy equations are approximated by a finite-difference method, and the radiative transfer equation is discretized by the product-integration method in which the shape function is taken to be piecewise-constant. The numerical grid for the radiation field is matched with the flowfield grid, and the continuity, momentum, and energy equations are coupled with the radiative transfer equation to obtain steady-state solutions. The model is verified by comparison with existing solutions for a laminar Poiseuille flow. Some sample calculations of inviscid supersonic flow of an ideal gas through a two-dimensional diffuser are presented to show the effect of radiation on the temperature field in the diffuser.

Nomenclature

a = absorption coefficient
A_r = aspect ratio
C = specific heat
e_g = blackbody emissive power of flow medium
e_s = blackbody emissive power of boundary surface
g = acceleration due to gravity
I = specific internal energy
k = extinction coefficient
K = kernel function, defined in Eq. (10)
$M+1$ = number of terms used in expansion of scattering phase function, for linear anisotropic scattering $M=3$
n, n' = inward unit normal vector of boundary surface
N = conduction-radiation parameter
N_b = number of boundary elements
N_d = number of volume elements
p = pressure
P_e = Peclet number
q_c = conductive heat flux
q_r = radiative heat flux from flow medium
q_s = radiative heat flux from boundary surface
r, r' = position vectors of computational cell
R = gas constant
R_{rad} = radiation-convection parameter
s = scattering coefficient
$S_i(\theta)$ = basis functions used in expansion of the scattering phase function; $i=0,\ldots,M$
t = time
T = temperature
u = x component of velocity
v = y component of velocity
$w_i(r)$ = functions defined in Eqs. (11)
α = thermal diffusivity
β_i = coefficients of linear anisotropic scattering
ϵ = surface emissivity
$\zeta_j(r)$ = interpolating function used in Eqs. (17)
λ = second coefficient of viscosity
λ_c = thermal conductivity
μ = first coefficient of viscosity
$\xi_j(r)$ = interpolating function used in Eqs. (17)
π = stress tensor
ρ = density
Σ = boundary of computational domain
σ = Stefan-Boltzmann constant
τ_o = optical thickness
Ψ = directional angle
ω_0 = scattering albedo, $\equiv s/(s+a)$
Ω = computational domain

Presented as Paper 89-0602 at the AIAA 27th Aerospace Sciences Meeting, Reno, NV, Jan. 9-12, 1989; received Feb. 21, 1989; revision received July 20, 1989.

*Research Engineer, Department of Mechanical Engineering; currently, University of Tennessee Space Institute, Tullahoma, TN.
†Associate Professor, Department of Mechanical Engineering; currently, Department of Aerospace Engineering and Engineering Mechanics.
‡E. C. H. Bantel Professor, Department of Mechanical Engineering. Associate Fellow AIAA.

Introduction

MOST previous investigations of combined heat transfer from a radiatively participating gray fluid were one-dimensional analyses. In many practical applications, this approximation is too crude to provide quantitative predictions. More recently the effects of two-dimensional radiation, diffuse gray boundaries, and isotropic scattering have also been studied,[1-4] but none of the investigations included all these effects simultaneously. Kassemi and Chung[5] studied the combined effects for a fully developed incompressible flow; the velocity field was known and uncoupled from the temperature field.

In this work we examine the combined effects of convective and radiative heat transfer from an absorbing, emitting, and scattering gray fluid subject to a two-dimensional radiation field. The energy equation is coupled with the momentum and continuity equations to obtain self-consistent velocity and temperature fields. The numerical solution of the radiative transfer equation used in this study is based on the formulation developed by Tan.[6] The product-integration method[7] is applied to discretize the integral equations to reduce the number of integrations, and irregular physical domains are transformed to regular computational domains. This significantly reduces the computational effort in numerical integration. Hence, the numerical grid for the radiation field can be matched with that for the flowfield, and solutions to the coupled continuity, momentum, and energy equations can be obtained with reasonably short computational time. The zone

method described by Kassemi and Chung[5] is similar to our method. However, their procedure is less general because the energy equation was uncoupled from the mass and momentum equations. Additionally, they did not treat an irregular physical domain or anisotropic scattering.

Formulation

The equations describing a two-dimensional flowfield of an emitting, absorbing, and scattering gray medium in local thermodynamic equilibrium are given below for convenient reference. Chemical and atomic reactions have been neglected.

Momentum Equations:

$$\frac{\partial \rho u}{\partial t}+\frac{\partial \rho u^2}{\partial x}+\frac{\partial \rho uv}{\partial y}=-\frac{\partial p}{\partial x}+\frac{\partial \pi_{xx}}{\partial x}+\frac{\partial \pi_{xy}}{\partial y}+\rho g_x \tag{1}$$

$$\frac{\partial \rho v}{\partial t}+\frac{\partial \rho uv}{\partial x}+\frac{\partial \rho v^2}{\partial y}=-\frac{\partial p}{\partial y}+\frac{\partial \pi_{xy}}{\partial x}+\frac{\partial \pi_{yy}}{\partial y}+\rho g_y \tag{2}$$

Continuity Equation:

$$\frac{\partial \rho}{\partial t}+\frac{\partial \rho u}{\partial x}+\frac{\partial \rho v}{\partial y}=0 \tag{3}$$

Equation of State (ideal gas):

$$p=\rho RT \tag{4}$$

Thermal Energy Equation:

$$\frac{\partial \rho I}{\partial t}+\frac{\partial \rho Iu}{\partial x}+\frac{\partial \rho Iv}{\partial y}=-p\left(\frac{\partial u}{\partial x}+\frac{\partial v}{\partial y}\right)+\frac{\partial}{\partial x}(\pi_{xx}u+\pi_{xy}v)$$
$$+\frac{\partial}{\partial y}(\pi_{xy}u+\pi_{yy}v)-\nabla\cdot q_c-\nabla\cdot q_r \tag{5}$$

The viscous stress tensor is defined by

$$\pi_{xx}=2\mu\frac{\partial u}{\partial x}+\lambda\left(\frac{\partial u}{\partial x}+\frac{\partial v}{\partial y}\right) \tag{6a}$$

$$\pi_{yy}=2\mu\frac{\partial v}{\partial y}+\lambda\left(\frac{\partial u}{\partial x}+\frac{\partial v}{\partial y}\right) \tag{6b}$$

$$\pi_{xy}=\mu\left(\frac{\partial u}{\partial y}+\frac{\partial v}{\partial x}\right) \tag{6c}$$

The conductive and radiative energy fluxes in the medium are q_c and q_r, respectively.

The radiative transfer term in the energy equation makes computations difficult because it turns the differential equation into an integro-differential equation. Tan has recently developed a new formulation for multidimensional radiative transfer in an emitting, absorbing, and anisotropic scattering medium with a gray boundary and constant (wavelength and temperature independent) properties.[6] In this case the radiative heat flux term ($\nabla\cdot q_r$) can be obtained from the integral equations for radiative heat transfer:

$$4e_g(r)-\frac{1}{a}\nabla\cdot q_r(r)=\int_\Omega K(r,r')\left[ke_g(r')-\frac{s}{4a}\nabla\cdot q_r(r')\right]\mathrm{d}V(r')$$
$$+\frac{s}{4}\sum_{k=1}^{M}\beta_k\int_\Omega K(r,r')w_k(r')S_k(\Psi)\,\mathrm{d}V(r')$$
$$+\int_\Sigma K(r,r')\left[e_s(r')-\frac{1-\epsilon}{\epsilon}q_s(r')\right]$$
$$\times\cos(r-r',n')\,\mathrm{d}A(r') \tag{7}$$

$$w_i(r)=\int_\Omega K(r,r')\left[ke_g(r')-\frac{s}{4a}\nabla\cdot q_r(r')\right]S_i(\Psi)\,\mathrm{d}V(r')$$
$$+\frac{s}{4}\sum_{k=1}^{M}\beta_k\int_\Omega K(r,r')w_k(r')S_k(\Psi)S_i(\Psi)\,\mathrm{d}V(r')$$
$$+\int_\Sigma K(r,r')\left[e_s(r')-\frac{1-\epsilon}{\epsilon}q_s(r')\right]S_i(\Psi)$$
$$\times\cos(r-r',n')\,\mathrm{d}A(r'),\qquad i=1,\ldots,M \tag{8}$$

$$e_s(r)-\frac{1}{\epsilon}q_s(r)=\int_\Omega K(r,r')\left[ke_g(r')-\frac{s}{4a}\nabla\cdot q_r(r')\right]$$
$$\times\cos(r'-r,n)\,\mathrm{d}V(r')+\frac{s}{4}\sum_{k=1}^{M}\beta_k\int_\Omega K(r,r')w_k(r')S_k(\Psi)$$
$$\times\cos(r'-r,n)\,\mathrm{d}V(r')+\int_\Sigma K(r,r')$$
$$\times\left[e_s(r')-\frac{1-\epsilon}{\epsilon}q_s(r')\right]\cos(r-r',n')$$
$$\times\cos(r'-r,n)\,\mathrm{d}A(r') \tag{9}$$

Equations (7) and (8) apply to points r in the domain Ω, and Eq. (9) applies to points on the boundary Σ. The blackbody emissive power of the flow medium and the boundary are e_g and e_s, respectively, and q_s is the net radiative heat flux on the wall. The kernel K is defined by

$$K(r,r')=\frac{1}{\pi}\frac{e^{-k|r-r'|}}{(r-r')^2} \tag{10}$$

Linear anisotropic scattering ($M=3$) is a common first approximation in scattering studies, although it can only model limited anisotropy.[8] In principle, higher-order expansions ($M>3$) can be incorporated in a straightforward manner in this formulation, but the large matrices may make the scheme impractical. Higher-order expansions were not attempted in this work. The functions w_i ($i=0,\ldots,3$) have physical significance[6]; w_0 is the radiant intensity integrated over all solid angles, and the remaining w_i are the radiant heat fluxes in the three coordinate directions, i.e.

$$w_0=4e_g-\frac{1}{a}\nabla\cdot q_r \tag{11a}$$

$$w_1=(q_r)_x \tag{11b}$$

$$w_2=(q_r)_y \tag{11c}$$

$$w_3=(q_r)_z \tag{11d}$$

The first of Eqs. (11) is obtained by integrating the equation of radiative transfer over all solid angles. The $S_i(\Psi)$, $i=0,\ldots,3$, are defined by

$$S_0=1 \tag{12a}$$

$$S_1=\sin\theta\cos\phi \tag{12b}$$

$$S_2=\sin\theta\sin\phi \tag{12c}$$

$$S_3=\cos\theta \tag{12d}$$

where the direction vector Ψ has polar and azimuthal angles θ and ϕ, respectively. The coefficients of linear anisotropic scattering are $\beta_0=1$; $\beta_1=\beta_2=\beta_3=a_1$, where a_1 is the first coefficient in the expansion of the scattering phase function.[9] The coefficients depend on the wavelength of the radiation and the diameter and optical properties of the scatterers. The wave-

length dependence of all optical properties was neglected in this work. The values used may be regarded as wavelength averaged quantities.

Numerical Method

The radiative equation is discretized by using the product-integration method.[7] Equations (7-9) can then be written[6]:

$$4E_g - \frac{1}{a}Q_g = A_{00}\left(kE_g - \frac{s}{4a}Q_g\right) + \frac{s}{4}\sum_{k=1}^{M}\beta_k A_{0k}W_k + B_0\left(E_s - \frac{1-\epsilon}{\epsilon}Q_s\right) \tag{13}$$

$$W_i = A_{0i}\left[kE_g - \frac{s}{4a}Q_g\right] + \frac{s}{4}\sum_{k=1}^{M}\beta_k A_{ik}W_k + B_i\left(E_s - \frac{1-\epsilon}{\epsilon}Q_s\right), \qquad i = 1,\ldots,M \tag{14}$$

$$E_s - \frac{1}{\epsilon}Q_s = C_0\left(kE_g - \frac{s}{4a}Q_g\right) + \frac{s}{4}\sum_{k=1}^{M}\beta_k C_k W_k + D\left(E_s - \frac{1-\epsilon}{\epsilon}Q_s\right) \tag{15}$$

where

$$E_g = \begin{pmatrix}(e_g)_1\\(e_g)_2\\\cdots\\(e_g)_{N_d}\end{pmatrix}, \qquad Q_g = \begin{pmatrix}(\nabla\cdot q_r)_1\\(\nabla\cdot q_r)_2\\\cdots\\(\nabla\cdot q_r)_{N_d}\end{pmatrix} \tag{16a}$$

$$W_i = \begin{pmatrix}(w_i)_1\\(w_i)_2\\\cdots\\(w_i)_{N_d}\end{pmatrix}, \qquad i = 1,\ldots,M \tag{16b}$$

$$E_s = \begin{pmatrix}(e_s)_1\\(e_s)_2\\\cdots\\(e_s)_{N_b}\end{pmatrix}, \qquad Q_s = \begin{pmatrix}(q_s)_1\\(q_s)_2\\\cdots\\(q_s)_{N_b}\end{pmatrix} \tag{16c}$$

where N_d and N_b are the total number of interior and boundary cells, $A_{lm}(l,m=0,1,\ldots,M)$, $B_l(l=0,1,\ldots,M)$, $C_l(l=0,1,\ldots,M)$, and D are matrices with elements

$$(a_{lm})_{ij} = \int_\Omega K(r_i,r')\xi_j(r')S_l(\Psi)S_m(\Psi)\,dV(r') \qquad i,j=1,2,\ldots,N_d \tag{17a}$$

$$(b_l)_{ij} = \int_\Sigma K(r_i,r')\zeta_j(r')S_l(\Psi)\cos(r-r',n')\,dA(r') \qquad i=1,2,\ldots,N_d,\quad j=1,2,\ldots,N_b \tag{17b}$$

$$(c_l)_{ij} = \int_\Omega K(r_i,r')\xi_j(r')S_l(\Psi)\cos(r'-r,n)\,dV(r') \qquad i=1,2,\ldots,N_b,\quad j=1,2,\ldots,N_d \tag{17c}$$

$$(d)_{ij} = \int_\Sigma K(r_i,r')\zeta_j(r')\cos(r-r',n')\cos(r'-r,n)\,dA(r') \qquad i,j=1,2,\ldots,N_b \tag{17d}$$

Equations (13-15) can be written in matrix form,

$$\begin{pmatrix}4E_g - \frac{1}{a}Q_s\\W_1\\W_2\\\cdot\\\cdot\\W_M\\E_s - \frac{1}{\epsilon}Q_s\end{pmatrix} = \begin{pmatrix}A_{00} & A_{01} & \cdots & A_{0M} & B_0\\A_{10} & A_{11} & \cdots & A_{1M} & B_1\\A_{20} & A_{21} & \cdots & A_{2M} & B_2\\\cdot & \cdot & & \cdot & \cdot\\\cdot & \cdot & & \cdot & \cdot\\A_{M0} & A_{M1} & \cdots & A_{MM} & B_M\\C_0 & C_1 & \cdots & C_M & D\end{pmatrix}\begin{pmatrix}kE_g - \frac{s}{4a}Q_g\\\frac{s}{4}\beta_1 W_1\\\frac{s}{4}\beta_2 W_2\\\cdot\\\cdot\\\frac{s}{4}\beta_M W_M\\E_s - \frac{1-\epsilon}{\epsilon}Q_s\end{pmatrix} \tag{18}$$

The location of the center of the ith cell is r_i; $\xi_j(r')$ and $\zeta_j(r')$ in Eqs. (17) are interpolating functions. In the following calculations, the interpolating functions are chosen to be piecewise-constant, consistent with the finite-difference approximation used for the mass and momentum conservation equations.

The computing mesh in the physical domain consists of a two-dimensional mesh of quadrilateral cells in Cartesian coordinates. The irregular quadrilateral cells are transformed into squares in the computational domain. Hence, depending on the accuracy required, a four- or eight-point Gaussian quadrature can be used to reduce the effort of numerical integration and make the calculation of the radiation terms compatible with the meshes generated for flowfields with complicated geometry. Singular points in the integrations can be avoided by transforming the volume integral into an area integral or by using polar coordinates in the x-y plane.

The computational flow chart is shown in Fig. 1. The elements of matrices A_{lm}, B_l, C_l, and D are precalculated, and during the computation these elements can be stored and reused, as long as the geometry and optical properties are the

same. If the optical properties of system vary with temperature, the matrix elements must be recomputed periodically. RADMTX is the program computing the matrix elements. Both RADMTX and the Navier-Stokes solver share the same grid generator. For compressible flow systems with coupled continuity, momentum, and energy equations, the time-marching scheme is the most widely used method to reach a steady-state solution. At each time step or iteration, the divergence of the radiative heat flux [Q_g in Eq. (18)] is obtained by a simple matrix operation and is then used in the energy balance equation. We used SALE written by Amsden et al.[10] to solve the Navier-Stokes equations, since it is a general purpose code with well-written documentation. Two parts of SALE were modified: 1) a READ statement was inserted into the input section to read the elements of matrix A_{lm}, B_l, C_l, and D calculated by RADMTX; 2) the radiative flux term was added to the energy equation, and a CALL statement was inserted to call the routine solving the matrix equation [Eq. (18)]. These modifications can be readily incorporated into programs other than SALE.

Results and Discussion

The accuracy of the computational procedure was tested using a hydrodynamically fully developed laminar flow between parallel plates at different temperatures. This flow was studied by Kassemi and Chung.[5] In this case the energy equation and momentum equation are uncoupled. The boundary conditions on the temperature were set by prescribing the inlet temperature, the wall temperatures were fixed with the no-slip condition imposed at the walls, and the outlet temperature was given by the mixed mean temperature of the flow at the exit. The calculations were made using an 11×11 nonuniform grid. The parameters and assumptions used in the calculation were based on Ref. 5. The channel aspect ratio $A_r = H/L = 0.1$, $P_e = U_0 H/\alpha = 200$, $\epsilon = 1.0$, $\tau_o = kH = 0.5$, $\omega_0 = 0$, and $T_{\text{cold}} = 0.6\ T_{\text{hot}}$. Here H and L are the channel height and width, respectively; U_0 is the mean flow velocity, and the plate temperatures are T_{cold} and T_{hot}, respectively. The conduction-radiation parameter $N\ (\equiv \lambda_c/H\sigma T^3)$ was varied between 0.005 and 1; Fig. 2 shows the corresponding steady-state nondimensional temperature profiles at the midplane of the channel ($x = 0.5L$). The agreement with the results in Ref. 5 is excellent; the results of the two calculations cannot be distinguished on the figure. The effects of scattering albedo (ω_0) and wall emissivity (ϵ) were tested, and the results also showed good agreement with Ref. 5. Linear anisotropic scattering had negligible effect on the temperature field in this case.

In the remainder of this section, we present steady-state results for the effect of radiation on ideal gas flow through a two-dimensional supersonic diffuser with wedge angles of 10 deg. To our knowledge this is the first solution in which the two-dimensional continuity, momentum, and energy equations are solved simultaneously with the equation for radiative transfer. The following results illustrate the temperature fields only. This has been done partly to economize on space. More importantly, the results presented are more qualitative than quantitative because they were obtained by interpolation between points of a fixed 20×20 nonuniform grid that was densest near the wall. This grid is not well suited to resolve the oblique shocks in the flowfield whose locations are not known a priori (when the flowfield is strongly affected by radiation). Thus, quantitative computation would require a denser adaptive grid even for the inviscid flow computations. Detailed comparisons of changes in all flowfield variables are best made after a more accurate calculation is performed. Our objective here is to demonstrate the use of the technique, show the profound changes in the temperature field induced by strong radiative transfer, and motivate more accurate (and more expensive) computations.

The sample calculations are intended to demonstrate the capabilities of this technique. The maximum and minimum values of the parameters examined in this study are not the limits of computer codes; specific choices were made for a parametric study of the effects of several variables on the flowfield temperatures, but no attempt was made to run an exhaustive set. All the calculations were performed on a Cray XMP-24. The computational time ranged from a few seconds to tens of seconds depending on the initial guesses for the flow variables and the flow conditions. No attempt was made to optimize or vectorize the codes.

One disadvantage of the technique is the large amount of computer memory required. This limitation is common to all methods for solving the full radiative transfer equation because of the presence of a full matrix. Hence a very fine grid is prohibitive because of computer memory limitations. Thus this technique cannot easily resolve boundary layers in a flowfield. The following results were obtained using a 20×20 nonuniform grid for half the flowfield and exploiting symmetry about the centerline. Only convective terms were retained; in this approximation, viscosity and thermal conductivity are neglected so there is no thermal or momentum boundary layer.

In all these examples, the inlet flow is parallel with Mach number $M_0 = 3$. An ideal diatomic gas was used with constant ratio of specific heats ($\gamma = 1.4$), and all flow variables were nondimensionalized by their inlet values. The radiation boundary conditions at inlet and exit were set by assuming the

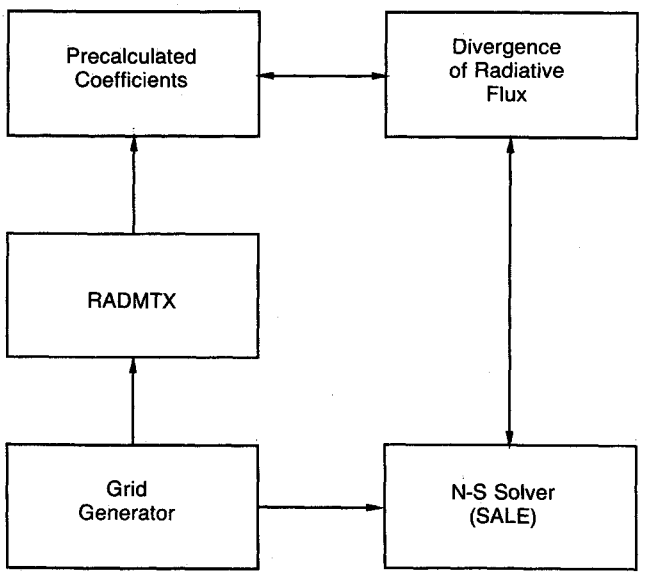

Fig. 1 Computational flow chart.

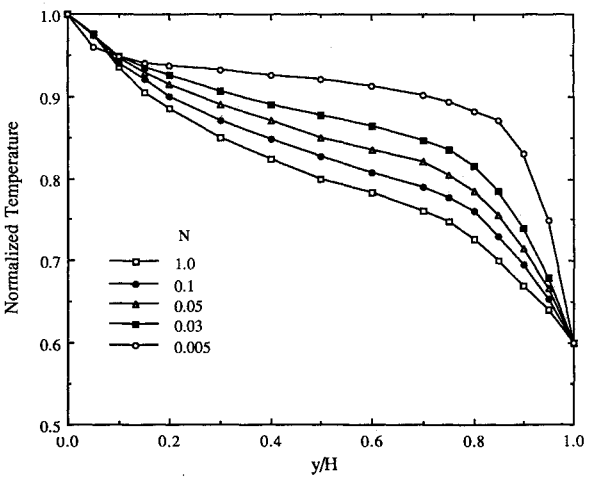

Fig. 2 Effect of conduction-radiation parameter (N) on temperature profiles.

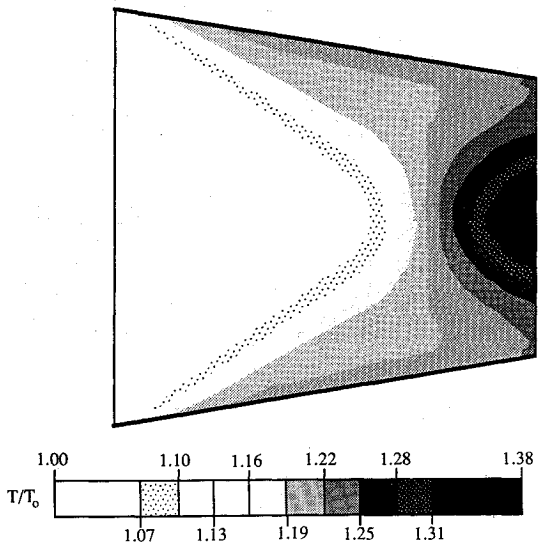

Fig. 3 Temperature field in a supersonic diffuser with uniform parallel inlet velocity, $M_0 = 3$, $R_{rad} = 0$ (no radiation).

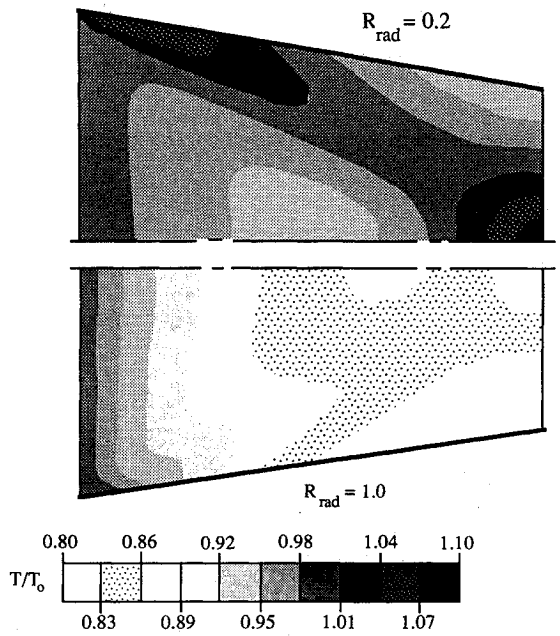

Fig. 4 Effect of a cold wall on the temperature field, $M_0 = 3$, $R_{rad} = 0.2$ and 1, $T_{wall} = 0.5T_0$, $\epsilon = 1$, $\tau_o = 1$, and $\omega_0 = 0$.

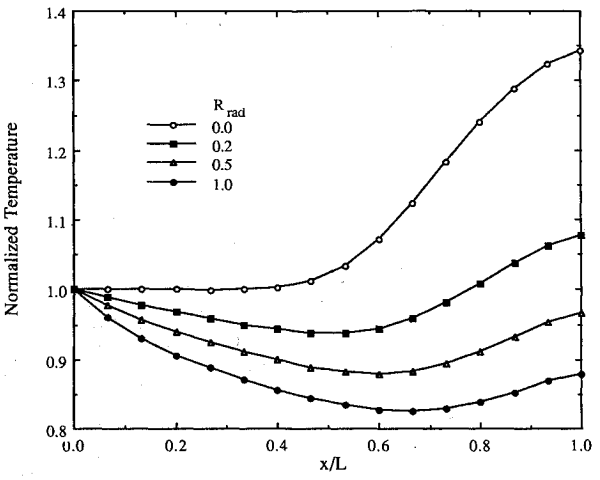

Fig. 5 Effect of R_{rad} on the centerline temperature.

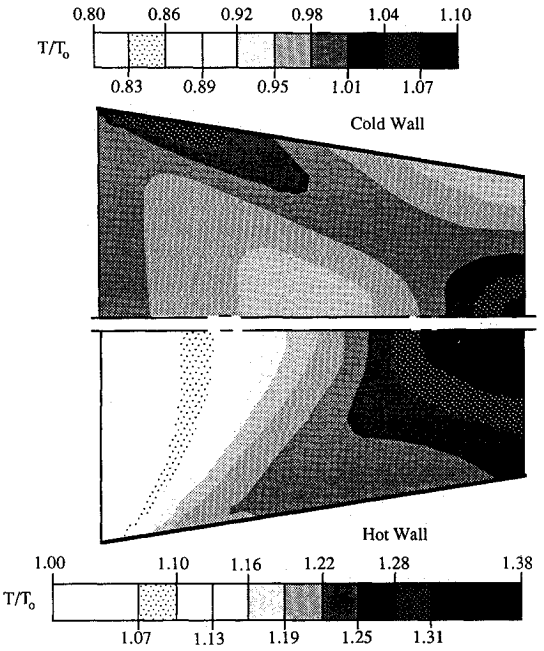

Fig. 6 Effect of a hot wall on the temperature field, $M_0 = 3$, $R_{rad} = 0.2$, $T_{wall} = 1.25T_0$, $\epsilon = 1$, $\tau_o = 1$, and $\omega_0 = 0$.

gas enters from a region at inlet temperature T_0 and discharges into a region at the same temperature as itself. Thus the radiation temperature at the exit T_{exit} is determined during the calculation. The wall emissivity ϵ, wall temperature T_{wall}, and optical thickness of the gas τ_o must be specified in addition. The optical thickness $\tau_o = kL$, where L is the length of the diffuser. The gas was assumed to be gray with a uniform constant absorption coefficient.

The computed temperature fields presented below are visualized using different dot density patterns. Approximately 10 readily distinguishable patterns were available; smaller increments in dot density were hard to distinguish within a single plot. Because of the relatively wide range of temperatures in the results, a single dot pattern could not be consistently associated with each temperature in all the figures. The density and temperature are strongly coupled in a compressible flow, and the locations of the shocks may generally be inferred from the location of steep temperature gradients.

The relative importance of radiation may be quantified by the radiation-convection parameter $R_{rad} \equiv \sigma T^3/\rho CU$; neglecting radiation is equivalent to setting $R_{rad} = 0$. The influence of radiation on the temperature field can be determined by comparison with a reference solution that neglects radiative transfer. The temperature rise in this flowfield is simply due to supersonic compression. Figure 3 shows the different temperature zones; the temperature contours were obtained by interpolation. The oblique shocks at the inlet and the reflected shocks may be inferred from the temperature contours. The thickness of the shocks is artificially increased because of the relative coarseness of the computational grid at the shock locations. As mentioned above, the grid was not adapted to optimize shock capture.

The temperature field when radiation is included in the computation is shown in Fig. 4 for moderate ($R_{rad} = 0.2$) and strong ($R_{rad} = 1$) radiative transfer. A cold wall was assumed, $T_{wall} = 0.5T_0$, with $\epsilon = 1$ and the optical depth of the gas $\tau_o = 1$. Note that the shading code starts from 0.80 instead of 1; hence the inlet is at a temperature near the middle of the scale. The shapes of the temperature contours in Fig. 4 are quite different from those in Fig. 3. The results show that as R_{rad} increases, the flow temperature decreases on the average, since radiative transfer from the main stream to the cold wall is enhanced. As a result, the local Mach number upstream of the oblique

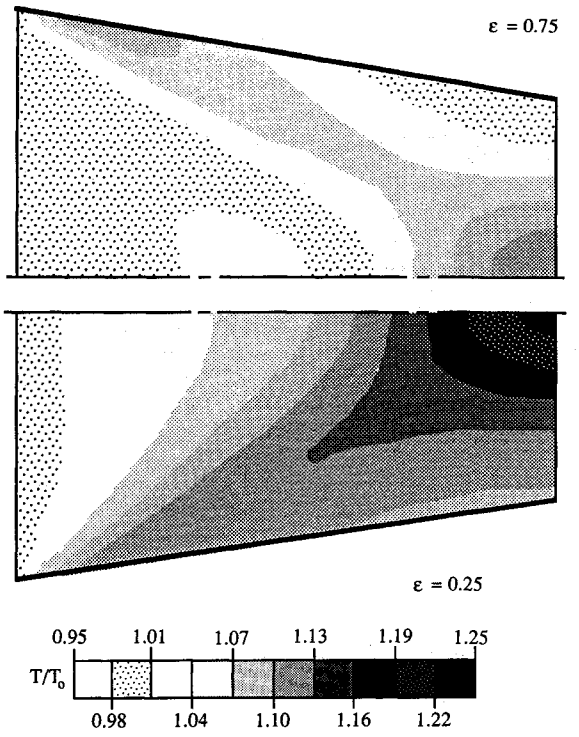

Fig. 7 Effect of surface emissivity on the temperature field, $M_0 = 3$, $R_{rad} = 0.2$, $T_{wall} = 0.5T_0$, $\epsilon = 0.75$ and 0.25, $\tau_o = 1$, and $\omega_0 = 0$.

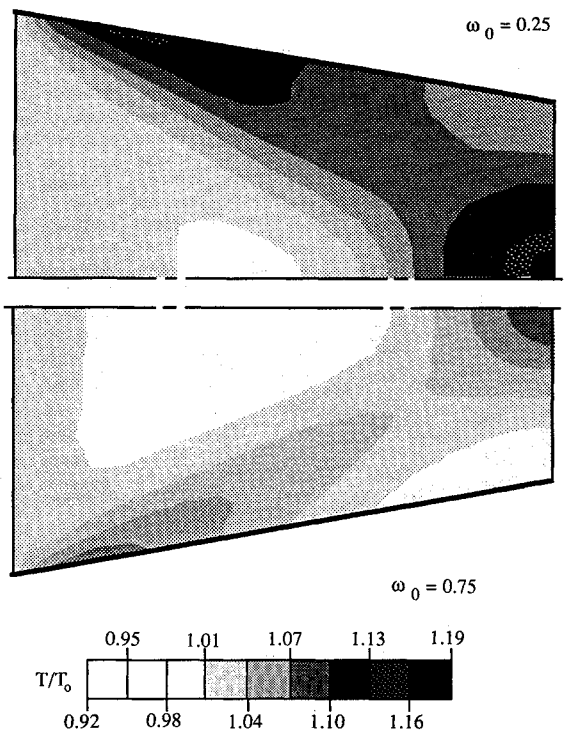

Fig. 9 Effects of isotropic scattering on the temperature field, $M_0 = 3$, $R_{rad} = 0.2$, $T_{wall} = 0.5T_0$, $\epsilon = 1$, $\tau_o = 1$, and $\omega_0 = 0.25$ and 0.75.

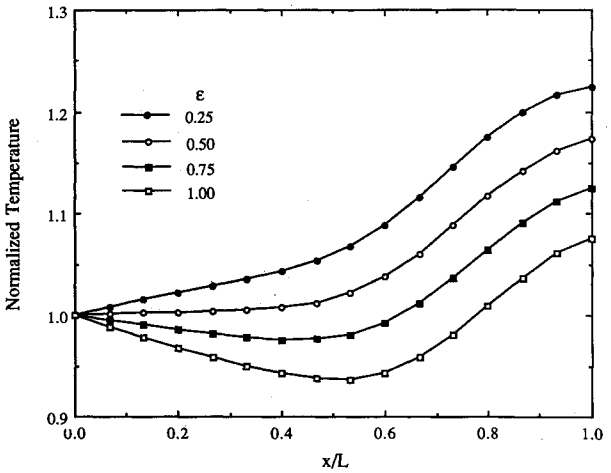

Fig. 8 Effect of surface emissivity on the centerline temperature.

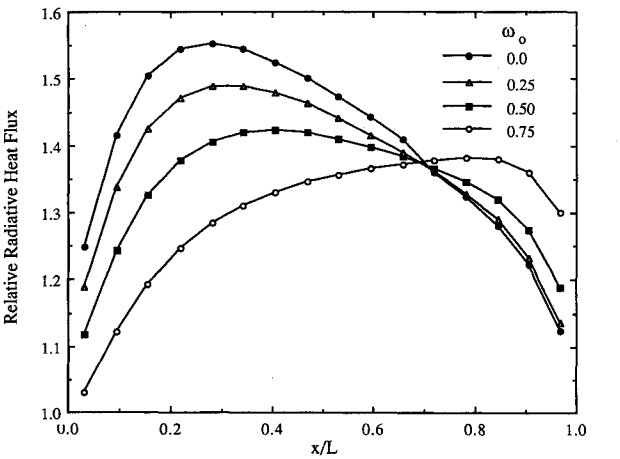

Fig. 10 Effect of isotropic scattering albedo ω_0 on the radiative flux on the boundary, $M_0 = 3$, $R_{rad} = 0.2$, $T_{wall} = 0.5T_0$, $\epsilon = 1$, and $\tau_o = 1$.

shocks is increased, and the shock angle decreased. The exit flow is substantially cooler than the inlet flow for $R_{rad} = 1.0$. Figure 5 shows the effect of R_{rad} on the centerline temperature for the cold wall case; increasing values of R_{rad} result in decreased centerline temperature as expected.

The relative effects of hot and cold walls on the temperature field are shown in Fig. 6. The $R_{rad} = 0.2$ (cold wall) part of Fig. 4 is repeated in Fig. 6 for easy comparison. The hot wall part of Fig. 6 shows the temperature field for $T_{wall} = 1.25T_0$ and other parameters held constant ($R_{rad} = 0.2$, $\epsilon = 1$, and $\tau_o = 1$). The shapes of the temperature contours are quite different in the two cases. The hot wall part of Fig. 6 may also be compared to Fig. 3. Radiant transfer from the hot wall and the downstream shocked gas preheats the upstream flow. This leads to lower local Mach number upstream of the shocks and greater shock angle than for the flowfield where radiation is insignificant.

The effect of surface emissivity on the temperature field was examined for a cold wall $T_{wall} = 0.5T_0$, with $R_{rad} = 0.2$, and $\tau_o = 1$. The results for $\epsilon = 0.75$ and 0.25 are contrasted in Fig. 7. The centerline temperature profiles for several values of ϵ are shown in Fig. 8. A smaller surface emissivity reduces the radiative loss to the cold wall from the main flow. Hence the decrease in gas temperature upstream of the oblique shock shown in the cold wall part of Fig. 6 ($\epsilon = 1$) is not as pronounced in the $\epsilon = 0.75$ part of Fig. 7. When the emissivity is decreased still further to $\epsilon = 0.25$, the gas upstream of the oblique shock is scarcely affected by the radiative loss to the wall and is instead heated because of radiative transfer from the shock-heated gases further downstream as indicated in the $\epsilon = 0.25$ part of Fig. 7. The shape of the temperature contours in the $\epsilon = 0.25$ part of Fig. 7 should be compared to those in Fig. 3 where radiative transfer from both the wall and the shock-heated gases were neglected.

Figures 9 compares the temperature fields for two different isotropic scattering albedos ($\omega_0 = 0.25$ and 0.75) for the cold wall case. Comparison of the $R_{rad} = 0.2$ part of Fig. 4 ($\omega_0 = 0$) with Fig. 9 (note scale differences) shows the enhanced scattering results in lower temperatures upstream of the oblique shock. This is because the energy radiated by the hot gas downstream of the shock is scattered away rather than being absorbed by the upstream gas. Figure 10 presents the radiative heat flux to the wall for various scattering albedos. As ω_0 increases, the surface upstream of the shock receives less energy while the heat flux to the downstream surface increases slightly. The reduction in the upstream surface heat flux is a result of the cooler upstream gases and reduced radiative transfer from the downstream gases because of scattering. The slightly enhanced downstream heat flux arises from backscattering of energy that would otherwise have been absorbed by the upstream gas.

Conclusions

We have constructed a general procedure for obtaining multidimensional steady-state solutions of the coupled mass, momentum, and energy equations with radiative transfer in an emitting, absorbing, and scattering fluid. The procedure was used to study the effects of some radiation parameters on a two-dimensional supersonic flowfield. Radiative transfer was shown to have significant influence on the temperature field and, by extension, on the other flow variables. The study demonstrates that it is possible to develop a computer code for multidimensional radiative transfer that can interface with the computational grids of codes adapted to purely convective flows. Tan's formulation permits rapid and efficient computation of the radiative transfer term. This should enable improved predictions of the performance of high tempearture devices. The principal disadvantage of the technique is the need for large amounts of computer memory. The technique can be extended using higher-order interpolating functions and wavelength dependent optical properties.

Acknowledgment

This research was supported by U.S. Department of Energy under Grant DE-FG05-87ER13735. We gratefully acknowledge helpful discussions with Z. Tan.

References

[1]Lii, C. C., and Özişik, M. N., "Heat Transfer in an Absorbing, Emitting and Scattering Slug Flow between Parallel Plates," *Journal of Heat Transfer,* Vol. 95, 1973, pp. 538–540.

[2]Chawla, T. C., and Chan, S. H., "Combined Radiation, Convection in Thermally Developing Poiseuille Flow with Scattering," *Journal of Heat Transfer,* Vol. 102, May 1980, pp. 297–302.

[3]Azad, F. H., and Modest, M. F., "Combinined Radiation and Convection in Absorbing, Emitting and Anisotropically Scattering Gas-Particulate Tube Flow," *International Journal of Heat and Mass Transfer,* Vol. 24, 1981, pp. 1681–1697.

[4]Chung, T. J., and Kim, J. Y., "Two-dimensional, Combined Mode Heat Transfer by Conduction, Convection, and Radiation in Emitting, Absorbing and Scattering Media-Solution by Finite Elements," *Journal of Heat Transfer,* Vol. 106, May 1984, pp. 448–452.

[5]Kassemi, M., and Chung, B. T. F., "Two-Dimensional Convection and Radiation with Scattering from a Poiseuille Flow," *Journal of Thermophysics and Heat Transfer,* Vol. 4, Jan. 1990, pp. 98–105.

[6]Tan, Z., "Radiative Heat Transfer in Multi-Dimensional Emitting, Absorbing and Anisotropic Scattering Media—Mathematical Formulation and Numerical Method," *Journal of Heat Transfer,* Vol. 111, Feb. 1989, pp. 141–147.

[7]Baker, C. T. H., *The Numerical Treatment of Integral Equations,* Clarendon, Oxford, UK, 1977, pp. 396–398.

[8]van de Hulst, H. C., *Multiple Light Scattering,* Academic, New York, 1980, p. 305.

[9]Chu, C. M., and Churchill, S. W., "Representation of Angular Distribution of Radiation Scattering by a Spherical Particle," *Journal of the Optical Society of America,* Vol. 45, Nov. 1955, pp. 958–962.

[10]Amsden, A. A., Ruppel, H. M., and Hirt, C. W., "SALE: A Simplified ALE Computer Program for Fluid Flow at All Speeds," Los Alamos National Laboratory, NM, LA-8095, June 1980.